

Full paper

Nickel-iron bimetallic diselenides with enhanced kinetics for high-capacity and long-life magnesium batteries

Limin Zhou^{a,b}, Fangyu Xiong^a, Shuangshuang Tan^a, Qinyou An^{a,*}, Zhaoyang Wang^a, Wei Yang^a, Zhanliang Tao^b, Yan Yao^{c,*}, Jun Chen^b, Liqiang Mai^{a,*}

^a State Key Laboratory of Advanced Technology for Materials Synthesis and Processing, Wuhan University of Technology, Wuhan 430070, Hubei, PR China

^b Key Laboratory of Advanced Energy Materials Chemistry (Ministry of Education), College of Chemistry, Nankai University, Tianjin 300071, PR China

^c Department of Electrical and Computer Engineering & Materials Science and Engineering Program, University of Houston, Houston, TX 77204, USA

ARTICLE INFO

Keywords:

Bimetallic diselenides

Magnesium batteries

Redox sites

Diffusion dynamics

ABSTRACT

Although Mg metal features high volumetric energy density and electrochemical dendrite-free deposition, Mg-storage cathode materials with desirable capacity and long-term stability have reached a bottleneck due to large diffusion barrier of Mg^{2+} . Herein, we report for the first time Ni-Fe bimetallic diselenides microflowers ($\text{Ni}_{0.75}\text{Fe}_{0.25}\text{Se}_2$, NFS) as cathode materials for rechargeable magnesium batteries. The NFS exhibits a considerable reversible capacity of 190 mAh g^{-1} and excellent Mg-storage cycling stability (148 mAh g^{-1} even after 500 cycles). Compared with unary transitional-metal diselenides (NiSe_2 , NS), the NFS shows more redox active sites and higher Mg^{2+} diffusion dynamics, contributing to superior reversible capacity and long cycle life. Furthermore, the concept of sequential reaction based on the potential discrepancy for the NFS magnesiation/demagnesiation process at steady stage was put forward and evidenced by electrochemical measurement and structural characterization. This paper paves the way for constructing advanced high-performance cathode materials of rechargeable magnesium batteries.

1. Introduction

Rechargeable magnesium batteries, as a potential energy storage system, have recently attracted considerable interest in beyond lithium-ion batteries (LIBs) owing to their overwhelming strength to exploit magnesium metal as anode material with high volumetric energy density (3833 mAh cm^{-3}) and electrochemical dendrite-free deposition [1–5]. Besides, magnesium (Mg) resources feature high abundance, low cost, and safety [1,2,6–8]. However, the development of desirable cathode materials is thwarted because of the polarizing nature of Mg^{2+} , tends to interact with the host to redistribute the charge on inserting and hopping, resulting in extremely sluggish diffusion dynamics of Mg^{2+} and large charge transfer hurdle [9–12]. Since the first Mg full battery prototype was reported in 2000 by Aurbach et al. [13], the endeavor to hit this pivotal breakthrough (Chevrel phase Mo_6S_8 delivering a capacity of 110 mAh g^{-1}) has validated challenging. Therefore, innovation for magnesium battery chemistry with high-capacity and cycle-stable cathode materials to reversibly intercalate Mg^{2+} is urgently needed.

To improve their electrochemical performance, recent efforts were devoted to viable alternative of oxides and chalcogenides [14–18]. With

regard to the mobility of Mg^{2+} , metal chalcogenide hosts are reported to show better performance for magnesium batteries, attributing to the weak interaction between soft anion lattice and Mg ions [15,19]. For example, Nazar's group successively presents layered TiS_2 and thiospinel ($\text{C-Ti}_2\text{S}_4$), delivering a capacity of 115 mAh g^{-1} and 140 mAh g^{-1} after 40 cycles at 60°C , respectively [20,21]. A certain amount of capacity has been increased via elevating temperature to overcome the migration barrier of Mg^{2+} diffusion. While the cycle life of cathodes still has a long way to go. Layered MoS_2 with an extended interlayer space ($\text{peo}_2\text{-MoS}_2$) demonstrated a capacity of 75 mAh g^{-1} , higher than commercial bulk MoS_2 (22 mAh g^{-1}) [22]. We can learn that the capacity of layered materials could allow a limited augment through interlayer expansion. Actually, few cathode materials currently enable Mg-storage performance to rival Mo_6S_8 due to double charge polarity and phase irrecoverability during repeated Mg^{2+} shuttling. With inspiration from our previous work on the superior electrochemical performance of binary transition-metal disulfides for sodium ion batteries [23], we want to know if bimetallic strategy enables magnesium battery system to relieve Mg^{2+} diffusion kinetics problem through potential discrepancy.

Herein, Ni-Fe bimetallic diselenides microflowers ($\text{Ni}_{0.75}\text{Fe}_{0.25}\text{Se}_2$,

* Corresponding authors.

E-mail addresses: anqinyou86@whut.edu.cn (Q. An), yyao4@uh.edu (Y. Yao), mlq518@whut.edu.cn (L. Mai).

<https://doi.org/10.1016/j.nanoen.2018.10.033>

Received 12 September 2018; Received in revised form 10 October 2018; Accepted 15 October 2018

Available online 17 October 2018

2211-2855/© 2018 Elsevier Ltd. All rights reserved.

NFS) were fabricated through facile solvothermal approach and successfully applied as cathode materials with enhanced diffusion kinetics for magnesium batteries. Impressively, the NFS delivers an outstanding reversible capacity of 190 mAh g^{-1} and possesses the capability to retain 148 mAh g^{-1} at a current density of 20 mA g^{-1} even after 500 cycles. The excellent Mg-storage performance is attributing to the bi-metallic effect, which induces more redox sites and higher Mg^{2+} diffusion dynamics compared with unary transitional-metal diselenides (NiSe_2 , NS). In addition, the mechanism of sequential reaction is proposed to account for the electrode behavior at steady stage, as evidenced by integrated techniques of spectroscopic characterization and electrochemical analysis. The results suggest the availability of bi-metallic strategy for the development of rechargeable magnesium battery with high capacity and long life span.

2. Results and discussion

The synthesis procedure of NFS involved the preparation of Ni-Fe layered double hydroxide (NiFe-LDH) (Figs. S1 and S2) and the selenylation of NiFe-LDH (Fig. S3) (details described in Experimental Section). For comparison, pure NiSe_2 microflowers (NS) were synthesized by identical process without the addition of ferric salts. Figs. 1a and S4 show the X-ray diffraction (XRD) patterns of the as-prepared NFS and NS samples. All diffraction lines of the NS are in good agreement with those of JCPDS No. 65–5016, indicating a cubic NiSe_2 with the space

group of Pa-3. While all the peaks of the NFS shift toward higher angle, in that the radius of ferrous ion is less than that of nickel ion. The resultant refined profile of the NFS shown in Table S1 indicates the preservation of cubic structure, in which Ni and Fe ions occupy 1/2 of the tetrahedral sites (4a) and Se ions reside 1/2 of the octahedral sites (8c) as well as the 1/4 probability for Fe ion to substitute Ni ion. Because of the ionic diameter of Fe^{2+} close to that of Ni^{2+} , so the ferrous ion was chosen as the cation-doping agent to form solid solution. Furthermore, the Raman spectra of the NFS becomes broader and migrates toward lower wave number compared with that of the NS (Fig. S5), which is attributed to the change of lattice space and variation of bond length, similar to the system of other cation-doping [24,25]. Fig. 1b and c present the typical scanning electron microscopy (SEM) images of the NFS, illustrating the nanosheets are self-assembled into uniform microflowers. The transmission electron microscopy (TEM) image (Fig. 1d) further reveals the interconnected nanosheets are composed of numerous nanograins. The high-resolution TEM (HRTEM) image shown in Fig. 1e clearly presents lattice fringe with neighboring interlayer distance of 0.260 nm , which can be ascribed to (210) crystal plane. Besides, the well crystalline character of the NFS can be verified from structural symmetry of luminous dots in the selected area electron diffraction (SAED) pattern (inset of Fig. 1e). The elemental mapping images of the NFS (Fig. 1f) evidence uniform distribution of Ni, Fe, and Se components. The pure NS possesses analogous microflower architecture with the lattice distance of 0.268 nm (Fig. S6), consistent with

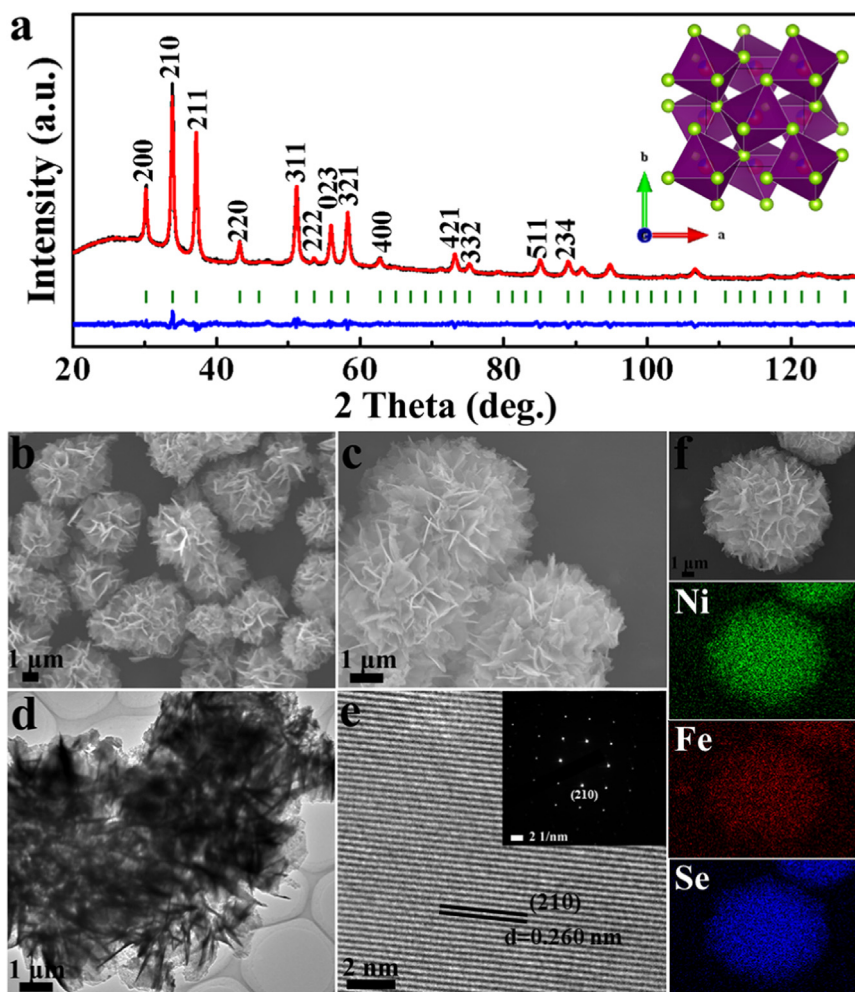


Fig. 1. Structural analysis and morphology characterization. (a) Rietveld refined XRD pattern of the NFS. Black curve – experimental data, red line – fitting data, vertical bars – Bragg diffraction positions, blue crosses – difference profile. Inset schematically represents the crystal structure of the NFS. (b, c) SEM, (d) TEM, (e) HRTEM images (inset displaying the corresponding SAED), and (f) elemental mapping images (Ni, Fe, Se) of the as-prepared NFS.

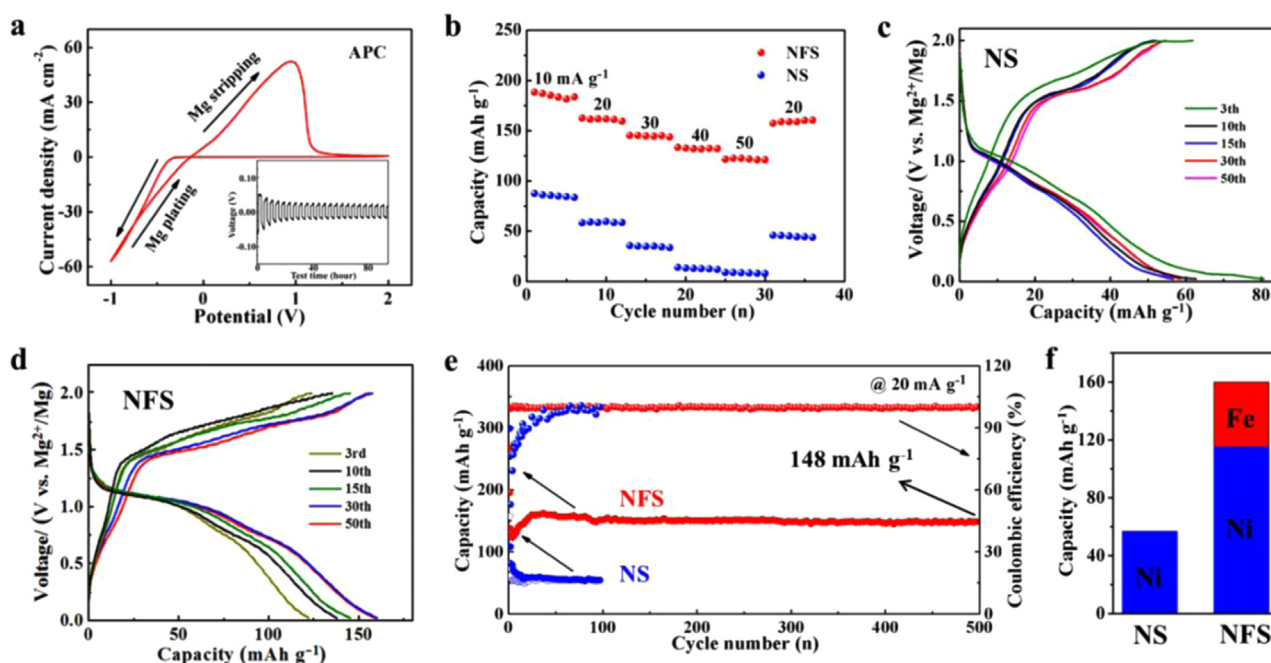


Fig. 2. Electrochemical performance. (a) Cyclic voltammograms of Mg electrode in APC electrolyte at a scan rate of 100 mV s^{-1} between -1.0 and 2.0 V , inset demonstrating galvanostatic cycling of symmetrical Mg//Mg cell at 0.02 mA g^{-1} . (b) Rate performance and (e) cycling performance at 20 mA g^{-1} of the NS and NFS electrode tested at room temperature (25°C). Charge/discharge curves of (c) NS and (d) NFS at 20 mA g^{-1} and 3rd, 10th, 15th, 30th, 50th cycle. (f) The proportion of capacity contribution of the Ni, Fe elements for the two electrodes.

the XRD comparison analysis.

The electrochemical properties of the NFS electrode were investigated at room temperature using 2032 coin cells with a Mg foil anode, all phenyl complex /tetrahydrofuran solution (APC) electrolyte, and glass fiber separator. The electrolyte, as an important component in magnesium batteries, was first evaluated. The excellent Mg stripping/plating efficiency and stability presented in Fig. 2a suggests APC electrolyte is available below 2 V . Fig. 2b shows the rate performance of the NFS and NS samples. The NFS delivers a reversible discharge capacity as high as 190 mAh g^{-1} when cycling at 10 mA g^{-1} . While there is only 88 mAh g^{-1} of discharge capacity for the NS electrode. With the current rate gradually increased to 50 mA g^{-1} , a reversible capacity of 120 mAh g^{-1} could be achieved for the NFS and almost no capacity is provided for the NS. It should be noted that the rate capacity was tested after 30 cycles in order to rationally justify kinetic performance. Fig. 2c displays the charge/discharge curves of the NS electrode cycled at 20 mA g^{-1} between 0.02 and 2.0 V . It can be seen that there is only one sloping plateau appeared for the NS electrode and the polarization is extremely large. However, there are two discharge voltage plateau of 1.15 and 0.90 V for the NFS at each cycle (Fig. 2d), indicating that two-step reactions appeared on Mg^{2+} insertion process due to the potential discrepancy between Ni^{2+} and Fe^{2+} . The NFS delivers a discharge capacity of 123 mAh g^{-1} at the 3rd cycle along with relatively small polarization. In addition, the capacities of the NFS electrode undergo an increasing trend at subsequent cycles, which are 135 , 145 , 157 , and 156 mAh g^{-1} at 10th, 15th, 30th, and 50th cycles, respectively. For long-term cycling stability, a capacity of around 148 mAh g^{-1} is attained even up to 500 cycles at 20 mA g^{-1} with a capacity retention of 98.2% calculated from 20th cycle (Fig. 2e). However, the capacity of the NS dramatically decreased to 60 mAh g^{-1} , analogous to the phenomenon literatures reported [6,14,15,21,26]. Considering the analogous microflower architectures, the discrepancy of Mg-storage performance for the NS and NFS electrodes could be attributed to the intrinsic crystal structural factor. For the NS electrode, the amount of involved- Mg^{2+} gradually decreases with the increasing of repulsive among two-charge Mg^{2+} and the interaction between host materials and

Mg^{2+} . While the NFS electrode based on the potential distinct of metal ion could create more redox active sites and improve the diffusion dynamics of cation and electron. With the exposure of more attacked sites, the capacity of the NFS electrode gradually increases during initial cycles. According to charge/discharge reaction process of NFS validated below, the proportion of capacity contribution for each metal is clearly illustrated in Fig. 2f, indicating that 25% of Ni substitution has endowed the whole system with triple the capacity of unary transitional-metal diselenides NiSe_2 . Compared with other metal oxides and chalcogenides, the capacity and cycle life of the NFS is remarkable when served as cathode materials for the promising magnesium battery technology (Table S2).

The solid-state diffusion coefficient of Mg^{2+} was studied with galvanostatic intermittent titration technique (GITT), which provides insights into the electrode kinetics through depth-of-discharge [27]. Based on potential response with time (Fig. S7), the Mg^{2+} diffusion coefficient could be calculated. It can be viewed from Fig. 3a and b that the average Mg diffusivity values ($D_{\text{Mg}^{2+}}$) of the NFS are about 2×10^{-10} and $8 \times 10^{-11} \text{ cm}^2 \text{ s}^{-1}$ on discharging and charging, respectively, which are typically one order of magnitude larger than that of $\text{C-Ti}_2\text{S}_4$, ($1-3 \times 10^{-11} \text{ cm}^2 \text{ s}^{-1}$) [20]. Moreover, there is a wave-shaped tendency for NFS electrode, indicating that Mg^{2+} diffusion dynamics accelerates and the redox sites gradually increase. In contrast, the NS electrode demonstrates a lower $D_{\text{Mg}^{2+}}$ ($3 \times 10^{-11} \text{ cm}^2 \text{ s}^{-1}$ and $5 \times 10^{-12} \text{ cm}^2 \text{ s}^{-1}$) and a larger polarization (Fig. S8). What's more, the Mg^{2+} diffusivity rate drastically dropped with continuous Mg^{2+} insertion, resulting from the increasing of repulsive force among multi-valence positive charge. As expected, the overpotential of the NFS electrode (100 and 120 mV) is only about one half of that of the NS (220 mV) (inset of Figs. 3a and S9). In addition of excellent ionic diffusion, the EIS analysis at various charge/discharge states shown in Fig. S10 illustrates the NFS also possesses favorable charge transfer compared with NS electrode. Thus it is gratifying that bimetallic approach enables cathode materials to relieve thorny kinetic issue involving Mg^{2+} mobility and electron transfer, realizing improved specific capacity and life span.

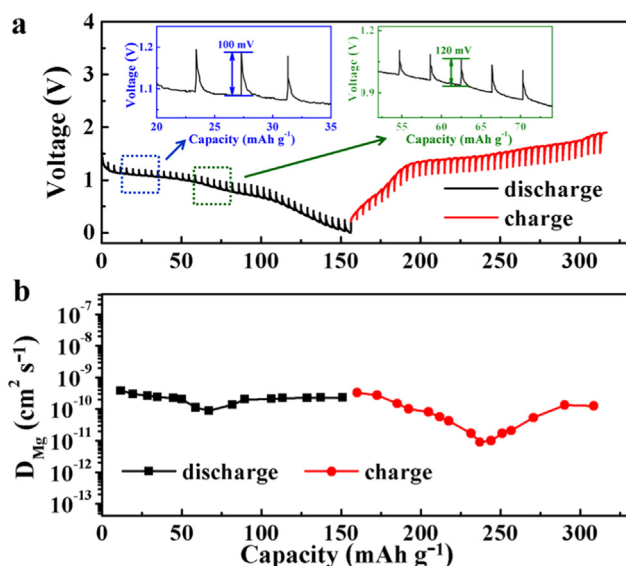


Fig. 3. Kinetic investigation. (a) GITT profiles and (b) calculated Mg^{2+} diffusion coefficient of the NFS electrode for the 30th cycle at 20 mA g^{-1} (inset demonstrating the magnification of rectangle region).

To track phase change of the NFS electrode at steady stage, *ex-situ* XRD measurements were conducted after 30 cycles (Fig. 4a). The ICP test was first adopted to determine the ratio of Ni to Fe, that is approximately 3:1. The diffraction peaks at 32.1, 43.8, and 49.3 are observed, analogy to the peak position of NiSe but with slight deviation, which could be assumed to be (101), (102), and (110) plane of $\text{Ni}_{0.75}\text{Fe}_{0.25}\text{Se}$. With the proceeding of continually discharging, the peaks of MgSe are found at 32.7, 47.0, and metallic Fe signal is vaguely

observed at 44.6, 49.4. On charging process, Fe species don't vanish when charging lower than 1.7 V, consistent with the reversed evolution on discharging stage. As charging to 2 V, $\text{Ni}_{0.75}\text{Fe}_{0.25}\text{Se}$ phase could be formed again. The phase transformation of selenide also emerged when CuSe_2 served as cathode material for magnesium batteries [26]. Besides, the failure to reveal the change of Ni species from XRD patterns probably is associated with highly dispersed discharge products into MgSe matrix, similar to Li/NiSe₂ system [28]. Fig. 4b shows the CV curve of the NFS electrode scanned at 0.5 mV s^{-1} after 30 cycles. There are two pairs of redox peaks observed, indicating a good reversibility of the NFS electrode at steady stage. In cathodic scan, two peaks at 0.72 and 1.03 V could be clearly distinguished, revealing a stepwise electrochemical conversion process. The typical charge profile similarly comprises two peaks, corresponding to Mg^{2+} gradual extraction. Instead, there is only one couple of redox peak found in the CV curve of the NS electrode (Fig. S11). To further elucidate two-step redox process of the NFS electrode, more evidence is unravel via *ex-situ* XPS spectra and HRTEM images at selected charge/discharge states (blue points marked in Fig. 4b). The high-resolution XPS spectra of Ni 2p_{1/2} (Fig. 4c) were fitted into Ni (2x) ($0 < x < 1$), Ni (II), and satellite peak, locating at 853.1, 857.3, and 862.2 eV, respectively [29]. Likewise, the peaks at 706.3, 709.8, and 715.1 eV of Fe 2p_{1/2} spectra are indexed to Fe (0), Fe (II), and satellite peak [30]. When discharged to 0.85 V, the emergence of Fe (0) peak suggests the Fe^{2+} is much easier to gain electron because of the relatively high working potential. With the proceeding of discharging to 0.02 V, a magnesian reaction takes place to generate NiSe_x based on the resultant XPS of Ni element. That's the reason why the reversible capacity is held at $\sim 148 \text{ mAh g}^{-1}$, lower than the theoretical capacity of NiSe (390 mAh g^{-1}). When charged to 1.7 V, the recordance of Ni (II) and Fe (0) illustrates that Ni^{2x+} has priority to lose electrons compared with Fe species. We can conclude that the Fe^{2+} was easier to be reduced on discharging and more arduous to be oxidized on charging than Ni^{2+} through comparative

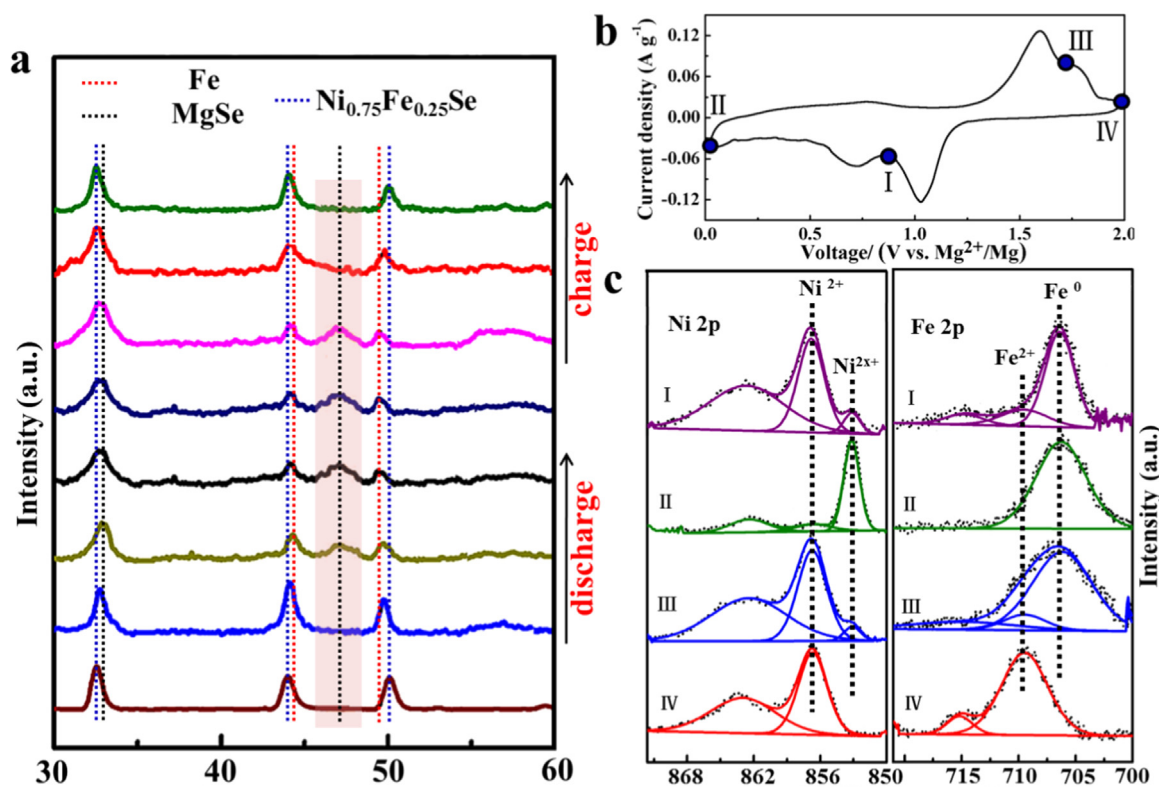


Fig. 4. Reaction mechanism at steady stage. (a) *Ex-situ* XRD patterns of the NFS electrode at various charge/discharge states. (b) CV curve of the NFS electrode scanning at 0.5 mV s^{-1} after 30 cycles. The points are marked for *ex-situ* analysis through dismantling the cells. Collected XPS profiles of high-resolution (c) Ni 2p and Fe 2p. The marks (I–IV) in (c) correspond to the marks in (b). All the samples were packaged with Kapton film in the glove box.

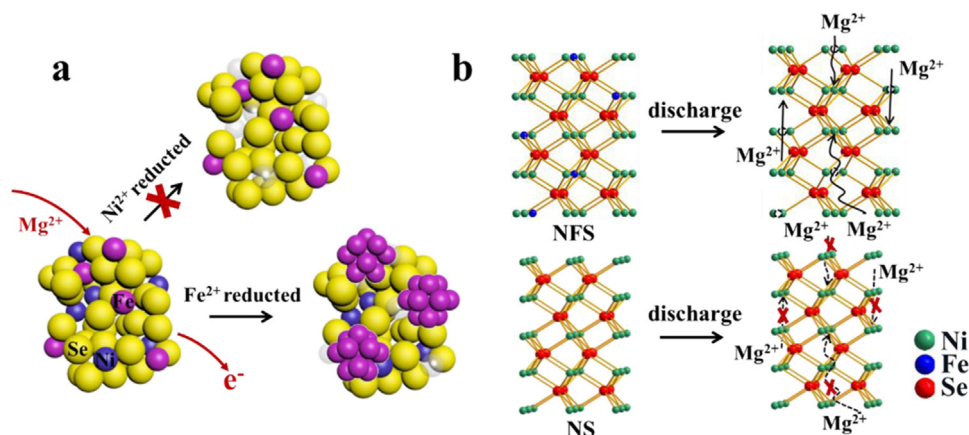


Fig. 5. (a) Schematic illustration of reaction order of Ni and Fe in the NFS electrode (blue ball is Ni ions, purple ball is Fe ions, yellow ball is Se ions, and purple cluster is elemental iron). (b) Comparison of increased redox sites of Ni-Fe bimetallic diselenide at steady stage with pure NiSe₂.

analysis. Integrated with the XRD resultant analysis of electrodes at different charge/discharge states, there is only Ni_{0.75}Fe_{0.25}Se involved in redox reaction at steady stage, and the electrochemical equation is Ni_{0.75}Fe_{0.25}Se + (1–0.75 ×)Mg²⁺ + (2–1.5 ×)e[–] ↔ 0.25Fe + 0.75 NiSe_x + (1–0.75 ×)MgSe, (0 < x < 1). Comparing the reaction nature of the NS and NFS conversion cathode, there exists redox reaction sequence for the NFS electrode, which spurs the exposure of more active sites and the improvement of cation diffusion dynamics as well as electron transfer. While the NS electrode just demonstrates the phase alternation and there is no defined order, so the capacity is relatively low and drastically attenuated. The speculation can be further visually illustrate via the HRTEM images and SAED patterns (Fig. S12). Moreover, the HAADF mapping images of fully discharged electrode demonstrate the uniform distribution of Ni, Fe, Se, and Mg elements and the preservation of nanosheet architecture on repeated electrochemical process (Fig. S13).

According to the above analysis on binary transitional-metal diselenides species, the redox order of the NFS electrode at steady stage is schematically presented in Fig. 5a. Upon initial magnesiation process, an irreversible conversion reaction emerges reflected by the transformation from Ni_{0.75}Fe_{0.25}Se₂ to Ni_{0.75}Fe_{0.25}Se phase. On further reversible magnesiation, Mg ions first react with Fe²⁺ to generate Fe and then with Ni²⁺ to form NiSe_x, evidenced by the resultant XRD and XPS characterization of the NFS electrode at various charge/discharge states. In the demagnesiation process, there exists an inverse electrode behavior of discharge reaction. As a result, the foremost generated Fe on discharge exerts much more channel to allow for Mg²⁺ shuttling along with more redox sites (Fig. 5b) as well as enhanced electronic conductivity. These superiorities obtained during charge/discharge process are favorable for relieving sluggish diffusion kinetics and achieving relatively high capacity and long cycle life.

3. Conclusion

In summary, we have demonstrated the first application of Ni-Fe bimetallic diselenides microflowers as a promising Mg-storage material with fast Mg²⁺ diffusion kinetics. The NFS electrode exhibits a considerable reversible capacity of 190 mAh g^{–1} and excellent cycling stability over 500 cycles with 148 mAh g^{–1} at 20 mA g^{–1}. Besides, the reaction mechanism of the NFS electrode at steady stage has been validated by the integration of electrochemical characterization, phase tracking, and spectrum analysis, in which Fe species were the first to be reduced on discharging and the last to be oxidized on charging, contributing to fast Mg²⁺ mobility and increased redox sites. These characters are favorable for significant electrochemical diffusion kinetics, further resulting in enhanced reversible capacity and long cycle life.

This study would shed light on further development of multi-metallic materials as cathode for high-performance multivalent-ion batteries.

4. Experimental section

4.1. Sample synthesis

The synthesis routine of Ni-Fe bimetallic diselenides microflowers (Ni_{0.75}Fe_{0.25}Se₂, denoted as NFS) involved the preparation of precursor Ni-Fe layered double hydroxide (NiFe-LDH) and the selenylation of NiFe-LDH through conventional solvothermal method with some modification [31–34]. In a typical procedure of LDH fabrication, a mixture of Ni(NO₃)₂·6H₂O (218 mg, 0.75 mmol), Fe(NO₃)₃·9H₂O (101 mg, 0.25 mmol), NH₄F (148 mg, 4 mmol), and CO(NH₂)₂ (360 mg, 6 mmol,) was dissolved in 24 mL deionized water, following by the addition of 12 mL ethylene glycol (EG). Afterwards, the above solution was transferred into Teflon-lined autoclave and heated at 120 °C for 12 h. The resulting kelly product was collected via washing with deionized water and ethanol and drying at 60 °C under vacuum. Then go on the key operation of selenylation of NiFe-LDH. Se powder (39 mg, 0.5 mmol) and NaBH₄ (38 mg, 1 mmol) were dispersed into 3 mL deionized water under ultrasonic. After thoroughly dissolution, 32 mL deionized water and 35 mg NiFe-LDH sample were successively immersed into the above solution and heated at 180 °C for 24 h in 50 mL Teflon-lined autoclave. The obtained black product was harvested via several rinsing and drying at 60 °C under vacuum. For comparison, pure NiSe₂ microflowers (NS) were synthesized by identical process without the incorporation of ferric salts.

4.2. Structure characterization

The structure of the as-obtained species was analyzed by a D8 Advance X-ray diffractometer (XRD) with Cu Kα radiation and Renishaw INVIA micro-Raman spectroscopy system. The XRD refinement of NFS was taken by RIETAN-2000 Rietveld program. The morphology and elemental distribution of the NiFe-LDH, NS, and NFS were characterized by field-emission scanning electron microscopy (FESEM, JEOL, JSM-7100F) and transmission electron microscopy (TEM, JEOL, JEM-2100F). The chemical states of elements were investigated by X-ray photoelectron spectroscopy (XPS, VG MultiLab 2000). The elemental content of the sample was determined by inductively coupled plasma atomic emission spectroscopy (ICP-AES, PerkinElmer Optima 8300).

4.3. Preparation of APC electrolyte

The all phenyl complex /tetrahydrofuran solution (APC, 0.25 M) was prepared in argon-filled glove box, in which there was phenyl magnesium chloride (PhMgCl) and aluminum chloride (AlCl₃, ultradry, 99.99%) used as solute. Specifically, 0.667 g AlCl₃ powder was slowly added into 15 mL tetrahydrofuran (THF, anhydrous, 99.9%) for stirring 12 h. Then 5 mL PhMgCl/THF solution (2 M) was slowly added dropwise into the above solution for 12 h of vigorous stirring. Thus, the mature APC electrolyte was obtained with multiple groups (e.g., Mg₂Cl³⁺, AlPh₂Cl²⁻, MgCl⁺) in the system.

4.4. Electrochemical measurements

The Mg battery properties were measured at room temperature (298 K) using CR2032 coin-type cells assembled in an argon-filled glove box. The working electrode was manufactured by grinding the as-prepared materials, acetylene black (AB), and poly(tetrafluoroethylene) (PTFE) with a weight ratio of 8:1:1 using isopropyl alcohol as solvent. Then the sticky dough was rolled into slice and cut into small dish with a diameter of 6 mm and a mass of ~2.0 mg. Glass fiber filter paper and Mg foil were used as the separator and anode, respectively. The all phenyl complex/tetrahydrofuran solution (APC) was employed as the electrolyte. Galvanostatic charge/discharge tests were performed between 0.02 and 2 V on a LAND CT2001A battery testing system. Electrochemical impedance spectroscopy (EIS) and cyclic voltammetry (CV) measurements were conducted on an Autolab electrochemical workstation. The Mg stripping/plating efficiency in APC electrolyte was evaluated by CV curves at a scan rate of 100 mV s⁻¹. The reversibility and stability of APC electrolyte were characterized by symmetrical Mg//Mg cells at 0.02 mA g⁻¹.

4.5. Calculation of diffusion coefficient by GITT measurements

The GITT was tested after 30 cycles to reasonably evaluate Mg²⁺ diffusion kinetics of the Mg/NFS cell. The cell stands for 30 min to make the voltage reach the real state and the pulse time lasts for 10 min at 20 mA g⁻¹. The cell system repeated above procedure until the charge/discharge process entirely completed. The diffusion coefficient of Mg²⁺ can be calculated according to the following equation:

$$D_{GITT} = \frac{4}{\pi\tau} \left(\frac{m_B V_M}{M_B S} \right)^2 \left(\frac{\Delta E_s}{\Delta E_\tau} \right)^2$$

where τ stands for current pulse time, m_B is the weight of active material, V_M and M_B are the molar mass (g mol⁻¹) and molar volume (cm³ mol⁻¹) of the active material, S is the contact area between electrode and electrolyte. As illustrated in Fig. S7, ΔE_s is the voltage difference of two successive steps measured at stable period in the open circuit voltage. ΔE_τ is the whole voltage change but the IR drop during the current pulse characterized.

Acknowledgements

This work was supported by the National Key Research and Development Program of China (2016YFA0202603), the National Basic Research Program of China (2013CB934103), the National Natural Science Foundation of China (51602239), the Natural Science Foundation of Hubei Province (2016CFB267), and the Fundamental Research Funds for the Central Universities (WUT: 2016III003, 2016IVA090, 2017III005).

Appendix A. Supporting information

Supplementary data associated with this article can be found in the online version at doi:10.1016/j.nanoen.2018.10.033.

References

- [1] J. Muldoon, C.B. Bucur, T. Gregory, Chem. Rev. 114 (2014) 11683–11720.
- [2] P. Canepa, G. Sai Gautam, D.C. Hannah, R. Malik, M. Liu, K.G. Gallagher, K.A. Persson, G. Ceder, Chem. Rev. 117 (2017) 4287–4341.
- [3] H.D. Yoo, I. Shterenberg, Y. Gofer, G. Gershinsky, N. Pour, D. Aurbach, Energy Environ. Sci. 6 (2013) 2265–2279.
- [4] C. Chen, J. Wang, Q. Zhao, Y. Wang, J. Chen, ACS Energy Lett. 1 (2016) 1165–1172.
- [5] S. He, K.V. Nielson, J. Luo, T.L. Liu, Energy Storage Mater. 8 (2017) 184–188.
- [6] N. Wu, Z.-Z. Yang, H.-R. Yao, Y.-X. Yin, L. Gu, Y.-G. Guo, Angew. Chem. Int. Ed. 54 (2015) 5757–5761.
- [7] Y. Shao, M. Gu, X. Li, Z. Nie, P. Zuo, G. Li, T. Liu, J. Xiao, Y. Cheng, C. Wang, J.G. Zhang, J. Liu, Nano Lett. 14 (2014) 255–260.
- [8] J. Luo, S. He, T.L. Liu, ACS Energy Lett. 2 (2017) 1197–1202.
- [9] Y. Liang, R. Feng, S. Yang, H. Ma, J. Liang, J. Chen, Adv. Mater. 23 (2011) 640–643.
- [10] H. Tian, T. Gao, X. Li, X. Wang, C. Luo, X. Fan, C. Yang, L. Suo, Z. Ma, W. Han, C. Wang, Nat. Commun. 8 (2017) 14083.
- [11] Y. Shao, Y. Shao, V. Raju, X. Ji, B.L. Mehdi, K.S. Han, M.H. Engelhard, G. Li, N.D. Browning, K.T. Mueller, J. Liu, Adv. Funct. Mater. 26 (2016) 3446–3453.
- [12] L. Zhou, Q. Liu, Z. Zhang, K. Zhang, F. Xiong, S. Tan, Q. An, Y.-M. Kang, Z. Zhou, L. Mai, Adv. Mater. 30 (2018) 1801984.
- [13] D. Aurbach, Z. Lu, A. Schechter, Y. Gofer, H. Gizbar, R. Turgeman, Y. Cohen, M. Moshkovich, E. Levi, Nature 407 (2000) 724–727.
- [14] L. Wang, K. Asheim, P.E. Vullum, A.M. Svensson, F. Vullum-Bruer, Chem. Mater. 28 (2016) 6459–6470.
- [15] W. Kaveevititchai, A.J. Jacobson, Chem. Mater. 28 (2016) 4593–4601.
- [16] L.F. Wan, J.T. Inconvati, K.R. Poeppelmeier, D. Prendergast, Chem. Mater. 28 (2016) 6900–6908.
- [17] B. Liu, T. Luo, G. Mu, X. Wang, D. Chen, G. Shen, ACS Nano 7 (2013) 8051–8058.
- [18] Y. Gu, Y. Katsura, T. Yoshino, H. Takagi, K. Taniguchi, Sci. Rep. 5 (2015) 12486.
- [19] Y. Wang, W.D. Richards, S.P. Ong, L.J. Miara, J.C. Kim, Y. Mo, G. Ceder, Nat. Mater. 14 (2015) 1026–1031.
- [20] X. Sun, P. Bonnicks, V. Duffort, M. Liu, Z. Rong, K.A. Persson, G. Ceder, L.F. Nazar, Energy Environ. Sci. 9 (2016) 2273–2277.
- [21] X. Sun, P. Bonnicks, L.F. Nazar, ACS Energy Lett. 1 (2016) 297–301.
- [22] Y. Liang, H.D. Yoo, Y. Li, J. Shuai, H.A. Calderon, F.C. Robles Hernandez, L.C. Grabow, Y. Yao, Nano Lett. 15 (2015) 2194–2202.
- [23] K. Zhang, M. Park, L. Zhou, G.H. Lee, J. Shin, Z. Hu, S.L. Chou, J. Chen, Y.M. Kang, Angew. Chem. Int. Ed. 55 (2016) 12822–12826.
- [24] J. Xia, X. Lu, W. Gao, J. Jiao, H. Feng, L. Chen, Electrochim. Acta 56 (2011) 6932–6939.
- [25] F. Long, J. He, M. Zhang, X. Wu, S. Mo, Z. Zou, Y. Zhou, J. Mater. Sci. 50 (2014) 1848–1854.
- [26] Y. Tashiro, K. Taniguchi, H. Miyasaka, Electrochim. Acta 210 (2016) 655–661.
- [27] Q. An, Y. Li, H. Deog Yoo, S. Chen, Q. Ru, L. Mai, Y. Yao, Nano Energy 18 (2015) 265–272.
- [28] M. Xue, Z. Fu, Electrochem. Commun. 8 (2006) 1855–1862.
- [29] G.-F. Chen, T.Y. Ma, Z.-Q. Liu, N. Li, Y.-Z. Su, K. Davey, S.-Z. Qiao, Adv. Funct. Mater. 26 (2016) 3314–3323.
- [30] Q. An, F. Lv, Q. Liu, C. Han, K. Zhao, J. Sheng, Q. Wei, M. Yan, L. Mai, Nano Lett. 14 (2014) 6250–6256.
- [31] H. Liang, L. Li, F. Meng, L. Dang, J. Zhuo, A. Forticaux, Z. Wang, S. Jin, Chem. Mater. 27 (2015) 5702–5711.
- [32] H.-S. Shim, V.R. Shinde, J.W. Kim, T.P. Gujar, O.-S. Joo, H.J. Kim, W.B. Kim, Chem. Mater. 21 (2009) 1875–1883.
- [33] S. Chen, J. Duan, M. Jaroniec, S.Z. Qiao, Angew. Chem. Int. Ed. 52 (2013) 13567–13570.
- [34] Z. Wang, J. Li, X. Tian, X. Wang, Y. Yu, K.A. Owusu, L. He, L. Mai, ACS Appl. Mater. Interfaces 8 (2016) 19386–19392.



Limin Zhou received her M.S. degree from College of Chemistry at Nankai University in 2015. She is currently working toward the Ph.D. degree in Materials Engineering from Wuhan University of Technology. Her current research focuses on synthesis and characterization of advanced materials for emerging energy storage devices.



Fangyu Xiong received his B.S. degree in Material Physics from Wuhan University of Technology in 2016. He is currently working toward the Ph.D. degree and his current research interest focuses on electrode materials for emerging energy storage devices.



Zhanliang Tao received his Ph.D. in Inorganic Chemistry from Nankai University in 2005. He has been an associated professor at the Key Laboratory of Advanced Energy Materials Chemistry (Ministry of Education) since 2008. His current research interests are focused on light weight nanomaterials for energy storage and conversion.



Shuangshuang Tan received his B.S. degree in Material Science and Engineering from Wuhan University of Technology in 2016. He is currently working toward the Ph.D. degree and his current research focuses on the energy storage materials and devices.



Yan Yao received his B.S. and M.S. degrees in Materials Science from Fudan University in 2000 and 2003. He received his Ph.D. in Materials Science and Engineering at University of California, Los Angeles in 2008. He went on working as a senior scientist at Polyera Corporation and then as a postdoctoral fellow at Stanford University. In 2012, he joined the University of Houston as an assistant professor. His research interests focus on magnesium/sodium ion batteries, aqueous batteries, and organic materials for energy storage. He has received the ONR Young Investigator Award (2013), Ralph E. Powe Junior Faculty Enhancement Award (2013) and Robert A. Welch Professorship (2012).



Qinyou An is Associate Professor of Materials Science and Engineering at Wuhan University of Technology (WUT). He received his Ph.D. degree from WUT in 2014. He carried out his postdoctoral research in the laboratory of Prof. Yan Yao at the University of Houston in 2014–2015. Currently, his research interest includes energy storage materials and devices.



Jun Chen is a Cheung Kong Scholar Professor, Director of Key Laboratory of Advanced Energy Materials Chemistry at Nankai University. He obtained his B.Sc. and M.Sc. degrees from Nankai University in 1989 and 1992, respectively, and his Ph.D. from Wollongong University (Australia) in 1999. He held the NEDO fellowship at National Institute of AIST Kansai Center (Japan) from 1999 to 2002. He has been working as a full professor on energy chemistry in Nankai University since 2002. His research activity focuses on nanostructured materials for electrochemical energy storage and conversion such as batteries, supercapacitors, fuel cells, and solar cells.



Zhaoyang Wang received his M.S. degree in Material Science and Engineering from Wuhan University of Technology (WUT) in 2016. He is currently working toward the Ph.D. degree and his current research focuses on the efficient non-noble metal catalysts for water splitting.



Liqiang Mai is Chair Professor of Materials Science and Engineering at Wuhan University of Technology (WUT). He received his Ph.D. from WUT in 2004. He carried out his postdoctoral research in the laboratory of Prof. Zhonglin Wang at Georgia Institute of Technology in 2006–2007 and worked as advanced research scholar in the laboratory of Prof. Charles M. Lieber at Harvard University in 2008–2011. His current research interests focus on nanowire materials and devices for energy storage. He received the National Natural Science Fund for Distinguished Young Scholars, the First Prize for Hubei Natural Science Award and so forth.



Wei Yang received his Master's degree in Materials Engineering from Wuhan University of Technology in 2017. He is currently a research assistant at Wuhan University of Technology. His research interests focus on developing functional materials for micro energy storage devices.